

Structural-Evolution Dynamics and Structural-Defect Suppression in High-Efficiency All-Polymer Solar Cells via Dilution Effect

Zhen Fu,¹ Tong Wang,¹ Wen-Qing Zhang,¹ Jia-Wei Qiao,¹ Feng-Zhe Cui,¹ Hang Yin¹,^{*}
Xiao-Yan Du¹,[†] Qin Wei¹,[‡] and Xiao-Tao Hao^{1,2,*}

¹*School of Physics, State Key Laboratory of Crystal Materials, Shandong University, Jinan 250100, China*

²*ARC Centre of Excellence in Exciton Science, School of Chemistry, The University of Melbourne, Parkville, Victoria 3010, Australia*

(Received 22 July 2023; revised 5 October 2023; accepted 17 October 2023; published 20 November 2023)

Structural defects in organic solar cells (OSCs) can significantly impact their performance by altering the density of the trap states and disrupting the energy-level alignment. These defects are primarily formed during the film-formation process, serving as intrinsic traps. In this study, we employed a dilution approach by blending an insulating polymer, polystyrene (PS), to control the structural-evolution process and reduce structural defects. By incorporating PS into two all-polymer systems, namely, PBDB-T:N2200 and PM6:PY-IT, the presence of enhanced stack ordering led to a reduction in structural defects, thus facilitating the charge-transfer process in all-polymer OSCs. However, this phenomenon was not observed in the nonfullerene system PM6:BTP-eC9. The compatibility between various components was examined in solution using both experiments and theoretical simulations, which revealed better miscibility between PS and the polymer materials. Our study demonstrates that the dilution effect of insulating polymers can effectively regulate the structural-evolution process and defects in organic semiconductors, resulting in enhanced performance of organic electronic devices.

DOI: 10.1103/PRXEnergy.2.043012

I. INTRODUCTION

Organic solar cells (OSCs) have attracted considerable attention due to their unique advantages of low-cost, flexibility, light weight, and so on [1–3]. The bulk heterojunction (BHJ) is the commonly used structure, with the active layer buffered by interfacial charge-transport layers as well as being sandwiched between the cathode and anode. Consisting of a donor and an acceptor, the active layer is one of the most important components for light absorption, charge generation, and transmission. The nonfullerene small molecule and polymer are two types of acceptors that are becoming popular [4–6]. Currently, the availability of high-efficiency nonfullerene acceptors (NFAs) has promoted the power-conversion efficiency (PCE) of single-junction OSCs to nearly 20% [7–12]. Nonfullerene small-molecular acceptors have their unique advantages, such as strong and

broader absorption in visible and near-infrared regions, an adjustable energy band gap, strong crystallinity, and orderly molecular stacking [13,14]. All-polymer solar cells have received attention in recent years for their long-term operational stability but their PCEs still lag behind those of the NFA-based OSCs [15–18]. Rapid advances in molecular design, morphology control, and device engineering have greatly enhanced the device performance of OSCs.

Trap states play a key role in determining the performance of OSCs. The sources of traps in OSCs can be divided into intrinsic and extrinsic traps. Structural defects are one type of intrinsic traps [19–21]. They originate from imperfections or impurities in the molecular structure and create energy levels inside the forbidden energy band gap, which will capture charge carriers that subsequently recombine with free carriers of the opposite sign [22–25]. Structural defects are mainly formed during the structural evolution of the film-formation process. The film-formation process can be modulated through a variety of methods [26,27]. Ma *et al.* have adopted ternary strategies to regulate the aggregate process for a more ordered molecular arrangement and higher crystallinity [28]. Yan *et al.* have selected 2-CF as an additive to effectively optimize the film-formation process, reduce trap-assisted recombination, and contribute to charge transport [29]. Blom *et al.*

*haoxt@sdu.edu.cn

Published by the American Physical Society under the terms of the [Creative Commons Attribution 4.0 International license](#). Further distribution of this work must maintain attribution to the author(s) and the published article's title, journal citation, and DOI.

al. have recently demonstrated that diluting transport sites can reduce the trap state density by fabricating diluted semiconductors with a wide-band-gap insulating polymer [30]. Insulating polymers have attracted broad attention as a low-cost material with great potential to effectively enhance π - π stacking, assist self-assembly, reduce the work function (WF) of electrodes, and thus optimize the performance of organic optoelectronic devices [31–34]. It is conceivable that blending of insulating materials leads to degradation of electrical properties but it has proven to be an important strategy for improving OSC performance [35]. However, the fundamental understanding of the effect of insulating polymers on the structural-evolution process and the density of the trap states in the active layer remains elusive.

In this work, we adopted the concept of diluting transport sites with insulating polymers to regulate the structural-evolution process and diminish structural defects. The insulating polymer polystyrene (PS) was selected as the model material blending into the active layer. We selected three representative systems, including PBDB-T:N2200, PM6:PY-IT, and PM6:BTP-eC9, as active layers. The changes in the structural-evolution dynamics, trap state density, molecular stacking, and device performance were observed after blending with PS. We found that the blending of PS can extend the film-solidification time to regulate the structural-evolution process, causes substantially improved crystallinity of the polymer blends, and contributes to the orderly arrangement of their molecular stacking for suppressed structural defects. Meanwhile, the miscibility among different components in solution was investigated by experiments and simulations to unravel the fundamental interaction mechanism of insulating polymer in the blends. The wetting coefficient and the Flory-Huggins interaction parameters were obtained using contact-angle measurements. The Gibbs free energy of different systems can be obtained by molecular-dynamics simulations. The results of the experiments and simulations indicate better miscibility between PS and polymer materials. Increased hole transfer rates and efficiencies were also observed and, finally, improved performance was achieved in all-polymer OSCs due to the blending of PS.

II. NANOSCALE MORPHOLOGY AND STRUCTURAL-EVOLUTION DYNAMICS

Figure 1(a) shows the energy-level diagrams of the donor materials PM6 and PBDB-T and the acceptor materials PY-IT, BTP-eC9, and N2200. The OSC devices were fabricated with the conventional structure to investigate the photovoltaic performance under AM 1.5G conditions [Fig. 1(b)]. Their molecular structures are shown in Fig. 1(c). BTP-eC9, as a narrow-band-gap

acceptor, is one of the most efficient OSC acceptor materials available. N2200, as a wide-band-gap polymer, has unique stability. PY-IT is polymerized from Y6, and its molecular structure has some similarities compared with BTP-eC9. The absorption spectra and photoluminescence (PL) spectra of each system are recorded in Figs. 1(d)–1(f) and in Fig. S1 of the Supplemental Material [36]. PS as an insulator does not participate in the energy-transfer process between the donor and the acceptor [10,37].

The grazing-incidence wide-angle x-ray scattering (GIWAXS) measurement was used to study the molecular packing and crystallinity in PBDB-T:N2200, PM6:PY-IT, and PM6:BTP-eC9 films. Figures 2(a)–2(f) and Figs. S2 and S3 of the Supplemental Material [36] show the 2D GIWAXS images and the corresponding line profiles of different blended films. For these blended films, (100) peaks are observed in the in-plane direction and (010) peaks are found in the out-of-plane direction, which suggests that all the blended films show a predominantly face-on orientation [38]. In addition, the crystalline coherence length (CCL), which is closely related to the charge transport and device performance, is extracted from the GIWAXS line profiles according to the Scherrer equation to quantify the molecular crystallinity, as summarized in Table S1 of the Supplemental Material [36]. In the PBDB-T:N2200 and PM6:PY-IT blending with PS, the CCL values associated with π - π stacking (010) are 1.78 Å and 2.04 Å, respectively, greater than for PBDB-T:N2200 and PM6:PY-IT binary blends (1.70 Å and 1.86 Å), while the CCL values in PM6:BTP-eC9 (2.69 Å) are slightly decreased to 2.56 Å with PS. Meanwhile, it can be observed that the CCL values of the all-polymer systems associated with lamellar stacking are also increased. The elongated CCLs indicate the increased crystallinity and more orderly stacking of molecules. The well-developed crystallinity is beneficial for the charge transport and therefore results in a higher fill factor (FF) and J_{SC} . We chose PM6 as a polymer donor to examine its crystallinity before and after the addition of PS. As depicted in Fig. S3 of the Supplemental Material [36], we found that the addition of PS enhances its crystallinity. Conversely, when it comes to the nonfullerene small molecule acceptor BTP-eC9, blending with the PS does not significantly improve its crystallinity. This observation aligns seamlessly with our discussion regarding the influence of PS on all-polymer organic solar cells. The nanoscale phase separation within the blended films was quantified through grazing-incidence small-angle scattering (GISAXS) measurements, with the 2D images shown in Fig. 2(g) and in Figs. S4(a)–S4(b) of the Supplemental Material [36] and the 1D profiles at the specular-beam position plotted in Fig. 2(h) and in Fig. S4(c) of the Supplemental Material [36]. To quantify and compare the phase separation in the nonfullerene

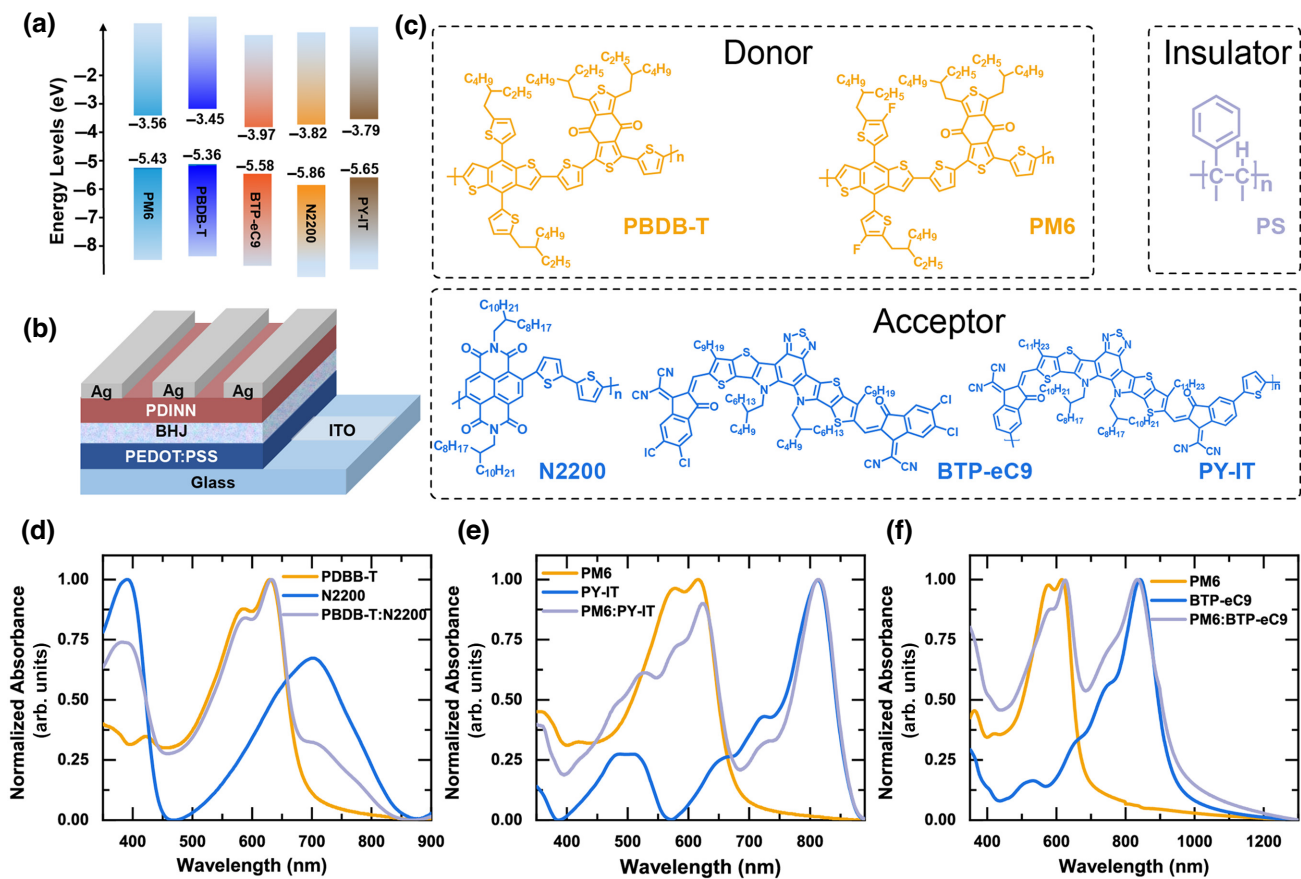


FIG. 1. (a) The energy-band diagrams of PM6, PBDB-T, PY-IT, BTP-eC9, and N2200. (b) A schematic diagram of the OPV device structure. (c) The molecular structures of PM6, PBDB-T, PY-IT, BTP-eC9, N2200, and PS used in the experiments. (d)–(f) The absorption spectra of various systems. ITO, indium tin oxide; PDINN, *N,N*-Bis{3-[3-(dimethylamino)propylamino]propyl}perylene-3,4,9,10-tetracarboxylic diimide; PEDOT:PSS, poly(3,4-ethylenedioxythiophene):poly(styrene-sulfonate);

photovoltaic blends, the 1D GISAXS profiles were fitted using a universal model, expressed as [39]

$$I(q) = \frac{A_1}{[1 + (q\xi)^2]^2} + A_2 P(q, R) S(q, R, \eta, D) + B. \quad (1)$$

The first term of the equation is the so-called Debye-Anderson-Brumberger (DAB) term, where q is the scattering wave vector, A_1 is an independent fitting parameter, and ξ is the average correlation length of the donor domain. The second term represents the contribution from fractal-like aggregations of acceptor. Here, $P(q, R)$ is the form factor of acceptor. $S(q, R, \eta, D)$ is the fractal structure factor, shown as [39]

$$S(q) = 1 + \frac{\sin[(D-1) \tan^{-1}(q\eta)]b \pm \sqrt{b^2 - 4ac}}{(qR)^D} \times \left[1 + \frac{1}{(q\eta)^2} \right]^{\frac{(D-1)}{2}}, \quad (2)$$

which describes the interaction between primary particles in this fractal-like aggregation system, where R is the mean radius of the primary acceptor aggregates and η is the correlation length of the fractal-like structure. The average correlation length of the clustered acceptor phases can be defined by the Guinier radius R_g of the network, where $R_g = \sqrt{(D(D+1)/2)\eta}$. In the blended films with PS, the ξ and $2R_g$ values are smaller than those of blended films without PS, suggesting the reduced donor-rich and acceptor-rich domain, which should be beneficial to efficient exciton dissociation in active layers [40]. As collected in Table S2 of the Supplemental Material [36], the data fitting suggests that the η values of PBDB-T and PM6 without PS are 54.83 nm and 62.88 nm, respectively, and that they decrease to 42.18 nm and 55.52 nm, respectively, after blending with PS, which indicates that blending with PS regulates the structural-evolution process during the film solidification. To further understand the crystallinity and phase-separation distinction induced by the introduction of PS, *in situ* ultraviolet-to-visible (UV-vis) absorption measurements were employed to illuminate the all-polymer aggregation process during

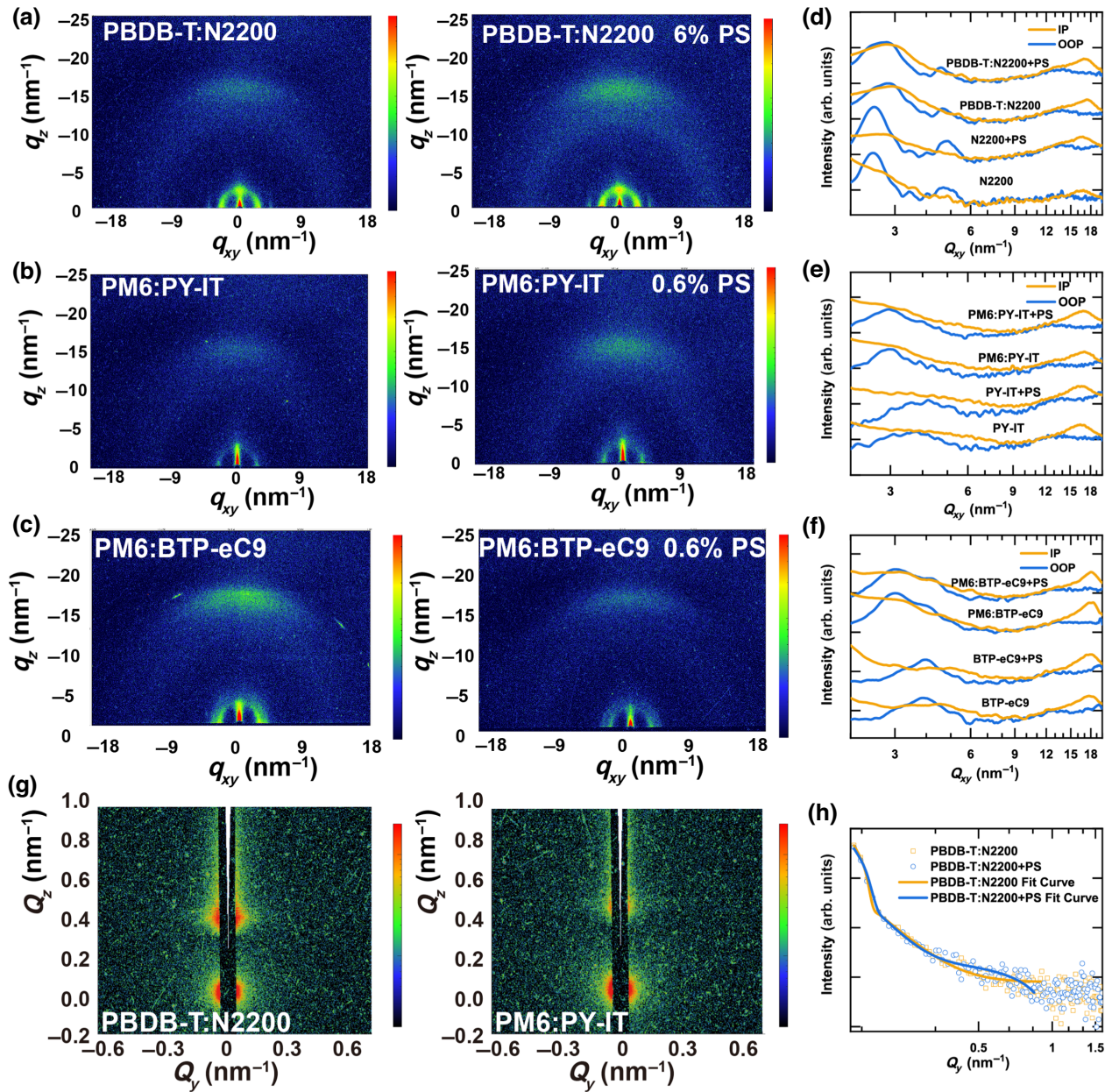


FIG. 2. (a)–(c) Two-dimensional (2D) GIWAXS patterns of (a) PBDB-T:N2200 and PBDB-T:N2200 with PS, (b) PM6:PY-IT and PM6:PY-IT with PS, and (c) PM6:PY-IT and PM6:PY-IT with PS. (d)–(f) One-dimensional (1D) profiles from GIWAXS patterns of (d) the N2200 system, (e) the PY-IT system, and (f) the BTP-eC9 system. (g) 2D GISAXS patterns of PBDB-T:N2200 and PM6:PY-IT. (h) 1D profiles from GIWAXS patterns of the N2200 system. IP, in plane; OOP, out of plane.

the film formation. The time evolution of the UV-vis contour maps is depicted in Figs. 3(a) and 3(b) and in Figs. S5(a) and S5(b) of the Supplemental Material [36]. The evolution of the peak intensity of the corresponding all-polymer systems with and without PS films is shown in Figs. 3(c) and 3(d) and in Figs. S5(c) and S5(d) of the Supplemental Material, respectively [36]. According to the evolution of the PBDB-T- and N2200-absorption peak intensity, the entire film-formation process can be divided into three stages. During the solution stage, as the spin coating starts, the peak intensity of

donors and acceptors gradually decreases and then, as the solvent evaporates, the peak intensity remains constant, indicating that aggregations of donors and acceptors have not started. In the solution-to-film transformation stage, the intensity of PBDB-T and N2200 is enhanced dramatically, which is attributed to the aggregation behavior during the solution-to-film transformation. The absorbances of the different systems at 400 and 800 nm were traced over time and correspond to the peak positions of the donor and acceptor. The results confirm the slower aggregation due to the blending with PS. Compared

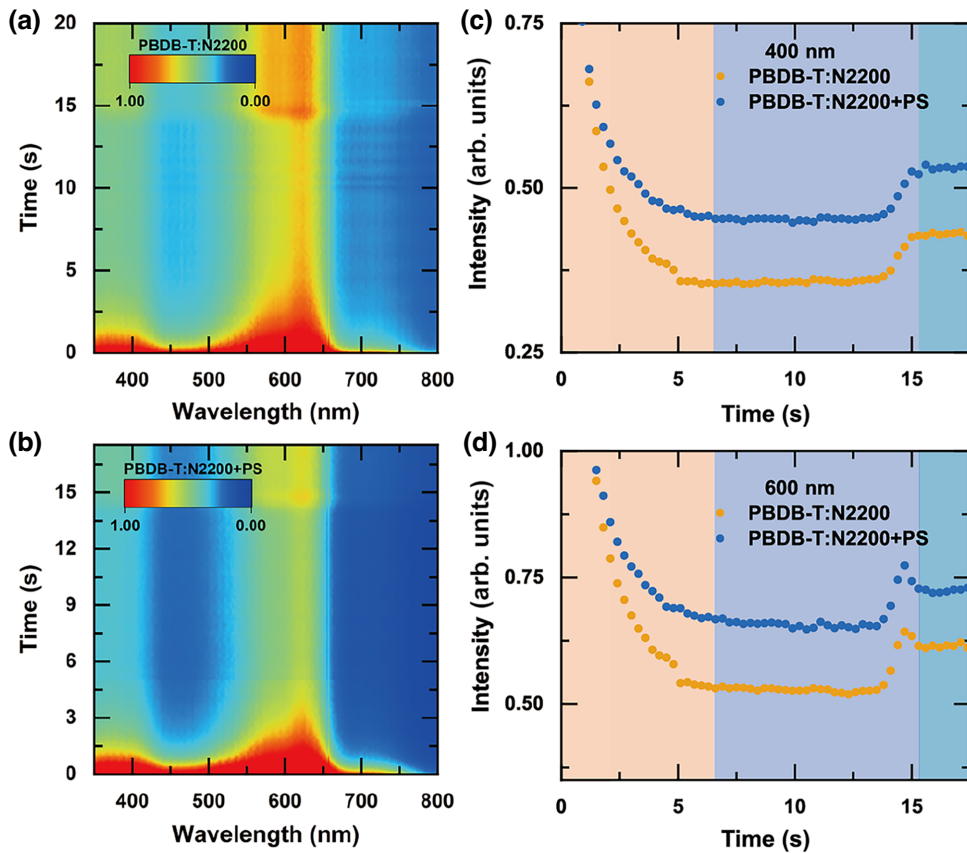


FIG. 3. (a),(b) Time-dependent contour maps of ultraviolet-to-visible (UV-vis) absorption spectra for (a) PBDB-T:N2200 and (b) PBDB-T:N2200 with PS. (c),(d) The time evolution of the peak intensity of (c) 600 nm and (d) 400 nm with different systems.

to PBDB-T:N2200, the much longer aggregation time of PBDB-T:N2200 with PS can provide enough time for the donor and acceptor to aggregate, nucleate, and crystallize, which facilitates reduction of the density of the trap states. Similar phenomena can be detected in PM6:PY-IT with and without PS. As the solvent evaporates further, the shift of the peak intensity stops, implying that the third stage is beginning. The peak intensity of the donors and acceptors remains constant over time at the third stage.

The influence of the PS on the surface morphology of the blended films was studied by using atomic force microscopy (AFM), as shown in Figs. 4(a)–4(c). After blending with PS, the surface of PM6:PY-IT and PBDB-T:N2200 films became much smoother (such as rms = 1.44 nm for the PM6:PY-IT film and rms = 1.08 nm after blending with PS). The distribution of PS in the blend is important for investigations of the effect of blending with PS and can be explored via the contact-angle measurement. To calculate the interfacial energy γ of the donor, acceptor, and PS, the definition of the free energy of adhesion and Young's equation are used to deduce [41,42]

$$\gamma_l(1 + \cos\theta) = 2\sqrt{\gamma_s^d\gamma_l^d} + \sqrt{\gamma_s^p\gamma_l^p}, \quad (3)$$

where γ_l and γ_s are the γ values of liquid-vapor and solid-vapor, respectively. γ^p and γ^d are the polar and dispersion components of γ , respectively ($\gamma = \gamma^p + \gamma^d$) and θ is the contact angle. The interfacial energy between components X and Y (γ_{XY}) is obtained through

$$\gamma_{XY} = \gamma_X - \gamma_Y - 2\sqrt{\gamma_X \times \gamma_Y} \times e^{-\beta(\gamma_X - \gamma_Y)^2}, \quad (4)$$

where β is 0.000115 m⁴ mJ⁻². According to the interfacial energy,

$$\omega_Z = \frac{\gamma_{ZY} - \gamma_{ZX}}{\gamma_{XY}} \quad (5)$$

is used in this work to calculate the ω_z value of material Z (PS) in a blend based on materials X (donor) and Y (acceptor).

The contact angles of the pure PY-IT, N2200, and BTP-eC9 are shown in Figs. 4(d)–4(f); others are shown in Fig. S6 of the Supplemental Material [36]. The corresponding surface energies are shown in Table I. The interface energy and wetting coefficient are summarized in Tables S3 and S4 of the Supplemental Material [36]. The different values of ω show that the PS can be located in different domains. If ω_z is larger than unity ($\omega_z > 1$), Z will be located in the

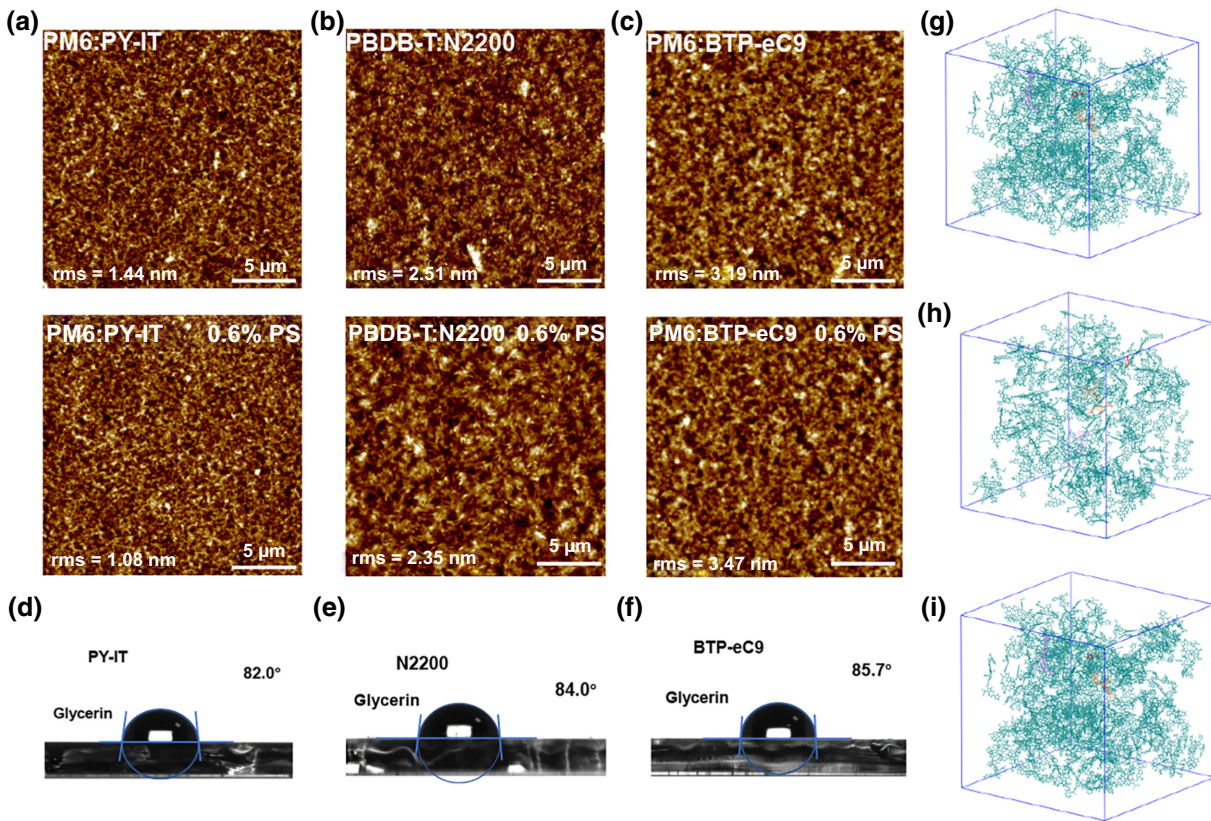


FIG. 4. (a)–(c) AFM images of (a) PM6:PY-IT, (b) PBDB-T:N2200, and (c) PM6:BTP-eC9 with PS. (d)–(f) Glycerin contact-angle images of (d) PY-IT, (e) N2200, and (f) BTP-eC9. (g)–(i) Molecular-dynamics simulations of (g) PBDB-T:N2200, (h) PM6:PY-IT, and (i) PM6:BTP-eC9.

domain of X . If $\omega_z < -1$, Z will be located in the domain of Y . If $-1 < \omega_z < 1$, Z will be located at the interface between X and Y [42]. As collected in Table I, for PM6 and BTP-eC9, ω is 1.42, which demonstrates that the PS is located in the donor domain. In contrast, for PM6:PY-IT and PBDB-T:N2200, ω is 0.38 and 0.09, respectively. This indicates that PS mainly acts at the donor and acceptor interface. The Flory-Huggins interaction parameter χ gives a measure of the interaction of the polymer chains with the small molecules as well as the polymer-polymer interaction. We can also use the Flory-Huggins interaction parameter χ to estimate the interaction and miscibility among different components. The χ values are calculated using the Hildebrand solubility parameters δ for materials with similar polarity according to

$$\chi = \frac{v_1}{RT} (\delta_i - \delta_j) + 0.34, \quad (6)$$

where $\delta_i = K\sqrt{\gamma_i}$, δ_i is the surface energy calculated via the contact angle, K is a proportionality constant simply given by $1.16 \times 10^5 \text{ m}^{-1/2}$, and v_1 is the molar volume of the solvent. The results are shown in Table S5 of the Supplemental Material [36]. The interaction parameters of $\chi_{PS,N2200}$ and $\chi_{PS,PY-IT}$ are 0.46 and 0.37, smaller

than for $\chi_{PS,BTP-eC9}$ (0.47), demonstrating better miscibility between PS and polymer materials compared to that between PS and BTP-eC9 [43].

The thermodynamic criterion can explain the relationship between the interface energy and the miscibility of different materials from their physical nature. The thermodynamic criterion for the blending of two-phase blended polymers is based on the following equation: $\Delta G = \Delta H_m - T\Delta S$, where ΔG is the mixed Gibbs free energy of the system and ΔS is the mixed entropy. The free enthalpy

TABLE I. The key parameters of the contact-angle measurements by using water and glycerol droplets.

Material	Contact angle			Hildebrand solubility parameter δ
	Water	Glycerin	Surface energy γ (mN m^{-1})	
PBDB-T	102.1	87.2	35.2	21.76
PM6	97.5	85.5	29.6	19.95
BTP-eC9	101.3	85.7	34.5	21.54
N2200	93.2	84.1	23.1	17.63
PY-IT	100.5	82.1	25.9	18.67
PS	100.7	83.1	28.6	19.61

(ΔH_m) per unit area of the interface is called the interfacial energy (γ). When $\Delta G < 0$, the two phases can be mixed into a thermodynamically stable homogeneous system. We use the coupling-parameter approach in conjunction with the thermodynamic integration (TI) formula to determine the mixed Gibbs free energy from [Figs. 3(g)–3(i)] [44,45]:

$$\Delta G_{AB} = \int_{\lambda_A}^{\lambda_B} \frac{\partial H(\lambda)}{\partial \lambda} d\lambda', \quad (7)$$

where the Hamilton H is a function of the coupling parameters. The dependence of the Hamiltonian defines a pathway connecting the two states of systems A and B . We can evaluate the ensemble average at multiple discrete points by performing a separate simulation for each selected point. The nonbonded interactions between A and B can be interpolated by

$$V_{ij}^{\text{nb}}(r) = (1 - \lambda) V_{ij}^A(r_{ij}^A) + \lambda V_{ij}^B(r_{ij}^B) \quad (8)$$

and

$$V_{ij}^A(r_{ij}^A) = \left(\frac{C_{ij}^{(12)}}{(r_{ij}^A)^{12}} - \frac{C_{ij}^{(6)}}{(r_{ij}^A)^6} \right) + f \frac{q_i q_j}{r_{ij}^A}, \quad (9)$$

$$(r_{ij}^B) = \left(\frac{C_{ij}^{(12)}}{(r_{ij}^B)^{12}} - \frac{C_{ij}^{(6)}}{(r_{ij}^B)^6} \right) + f \frac{q_i q_j}{r_{ij}^B}, \quad (10)$$

$$r_{ij}^A = \left(\alpha (\sigma_{ij}^A)^6 \lambda^2 + r_{ij}^6 \right)^{\frac{1}{6}}, \quad (11)$$

$$r_{ij}^B = (\alpha (\sigma_{ij}^A)^6 (1 - \lambda)^2 + r_{ij}^6)^{\frac{1}{6}}, \quad (12)$$

where $V^{\text{nb}}(r)$ is the soft-core potential, V_{ij}^A and V_{ij}^B are the potentials describing the nonbond interactions of two atoms in states A and B at a distance from r_{ij} , respectively, $C_{ij}^{(12)}$ and $C_{ij}^{(6)}$ are the interacting van der Waals parameters, the dispersive energy term, f , is equal to $1/4\pi\varepsilon_0$, and α is the soft-core parameter. Smaller mixed Gibbs free energy ΔG values imply an enhanced tendency toward miscibility. The ΔG values are -488.44 , -100.42 , and -75.55 kJ mol $^{-1}$ for PBDB-T:N2200, PM6:PY-IT, and PM6:BTP-eC9 with PS, respectively, which indicates the better miscibility between PS and polymer systems. The addition of PS modifies the interface between the donor and the acceptor, thus improving the crystallinity of the system. However, the poor miscibility of PS and BTP-eC9 locates PS in the donor domain rather than at the donor-acceptor interface for PM6:BTP-eC9 blends.

III. SUPPRESSING STRUCTURAL DEFECTS

The increased crystallinity of the system implies a more ordered arrangement of molecules [Fig. 5(a)] [38]. To

investigate whether ordered molecular stacking reduces the trap states, capacitance-frequency ($C-V$) measurements were further carried out to investigate the density of the trap states [46,47]. The measure was based on the capacitance-frequency dependence under changing applied bias (see Fig. S7 of the Supplemental Material [36]). Walter *et al.* have presented an analytical model that allows the energetic distribution of traps $N_t(E_\omega)$ to be determined from the measured capacitance-frequency data $C(\omega, T)$ [48]. The trap density of states at energy E_ω is related to the derivative of the capacitance with respect to the frequency as

$$N_t(E_\omega) = -\frac{V_{\text{bi}}}{qW} \frac{dC}{d\omega} \frac{\omega}{kT}, \quad (13)$$

where V_{bi} is the built-in potential and W is the width of the space-charge region. A Mott-Schottky plot is used to extract the built-in voltage V_{bi} and the apparent blending profile N_{ap} , which are calculated by

$$\frac{1}{C_j^2} = \frac{2(V_{\text{bi}} - V)}{q\varepsilon\varepsilon_0 N_{\text{ap}}} \frac{V_{\text{bi}}}{qW} \frac{dC}{d\omega} \frac{\omega}{kT}. \quad (14)$$

E_ω is calculated as follows:

$$E_\omega = kT \ln \left(\frac{2v_0}{\omega} \right). \quad (15)$$

As shown in Figs. 5(b) and 5(c) and in Fig. S8 of the Supplemental Material [36], the results reveal N_t values of 2.45×10^{17} cm $^{-1}$ eV $^{-1}$, 1.29×10^{17} cm $^{-1}$ eV $^{-1}$, 5.00×10^{18} cm $^{-1}$ eV $^{-1}$, and 2.25×10^{18} cm $^{-1}$ eV $^{-1}$ for PBDB-T:N2200, PBDB-T:N2200 with PS, PM6:PY-IT, and PM6:PY-IT with PS, respectively. Previous works have found that the use of ternary or other strategies to bring down the density of the trap states is accompanied by a change in the energy level of the trap states [47]. However, we find that the E_ω value of all-polymer systems does not change significantly after blending with PS but, rather, leads to a decrease in the overall trap-state density due to the more crystalline structure. Combined with the contact-angle and $C-V$ measurements, PS was found to be located between the donor and acceptor and to reduce the trap states in all-polymer systems, implying that PS suppresses the interfacial trap states. However, PS was located in the donor domain, without reducing the density of the trap states, for PM6:BTP-eC9, which is due to BTP-eC9, as a small molecule, being incompatible with PS. The density of the trap states is lowest for PBDB-T:N2200 with 6% PS and lowest for PM6:PY-IT with 0.6% PS, which may correspond to the best performance of the device. When the blending ratios reach 1% (PM6:PY-IT) and 10% (PBDB-T:N2200), the density of the trap states rises and exceeds that of the unblended device, because the crystallinity of

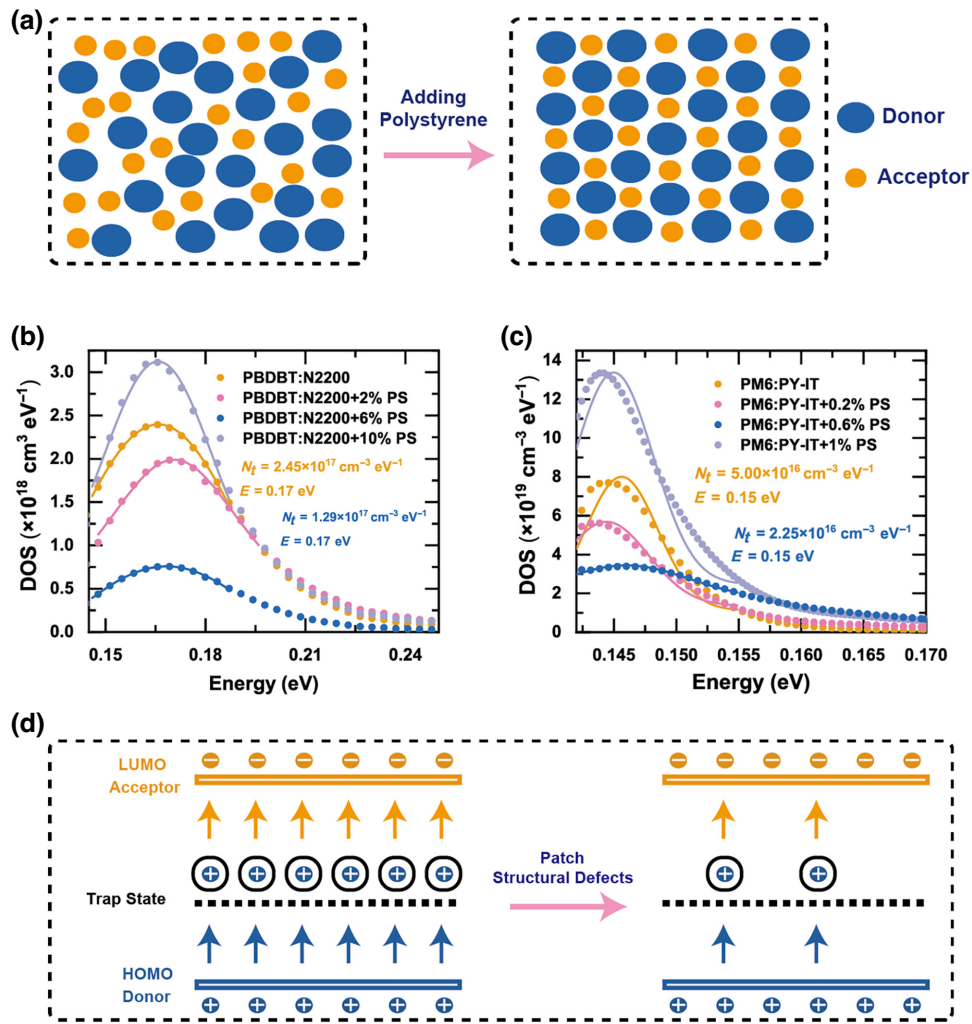


FIG. 5. (a) Molecular-stacking changes after the dilution effect. (b)–(d) The trap-state density of (b) PBDB-T:N2200 with PS, (c) PM6:PY-IT with PS, and (d) PM6:BTP-eC9 with PS. (e) The trap-assisted recombination process before and after suppressing structural defects. DOS, density of states.

the active layer is disrupted by the excessive blending of PS.

As is known, the traps in OSCs can originate from two sources, which are intrinsic and extrinsic traps, and structural defects are one type of intrinsic trap that have a significant impact on the performance of OSCs. The addition of PS can optimize the bulk heterojunction morphology and contribute to its increased crystallinity. Thus, structural defects are patched and the density of the trap states is suppressed [24]. Structural defects are not affected by temperature, so we performed low-temperature transient photo-current (TPC) measurements (see Fig. S9 of the Supplemental Material [36]). We found that the TPC change of the PY-IT system at low temperature and room temperature was not very obvious, while the decreasing trend was basically the same after adding PS. It is concluded that PS primarily suppresses structural defects

within the all-polymer system. As schematically shown in Fig. 5(d), trap-assisted recombination is a two-step process, where a hole is first trapped within the band gap and then recombines with an oppositely charged electron [22]. The addition of PS for dilution suppresses the structural defects, resulting in a significant reduction of the trap states and contributing to charge transport. The suppressed trap density can effectively prevent trap-assisted recombination and promotes the photogenerated carrier density of the active layer. Note that this phenomenon was observed in two all-polymer systems, PBDB-T:N2200 and PM6:PY-IT, but not in PM6:BTP-eC9, indicating that the suppression of blending structural defects due to insulating polymer mainly works in the all-polymer system.

According to the above measurement results, it can be speculated that PS can suppress structural defects between

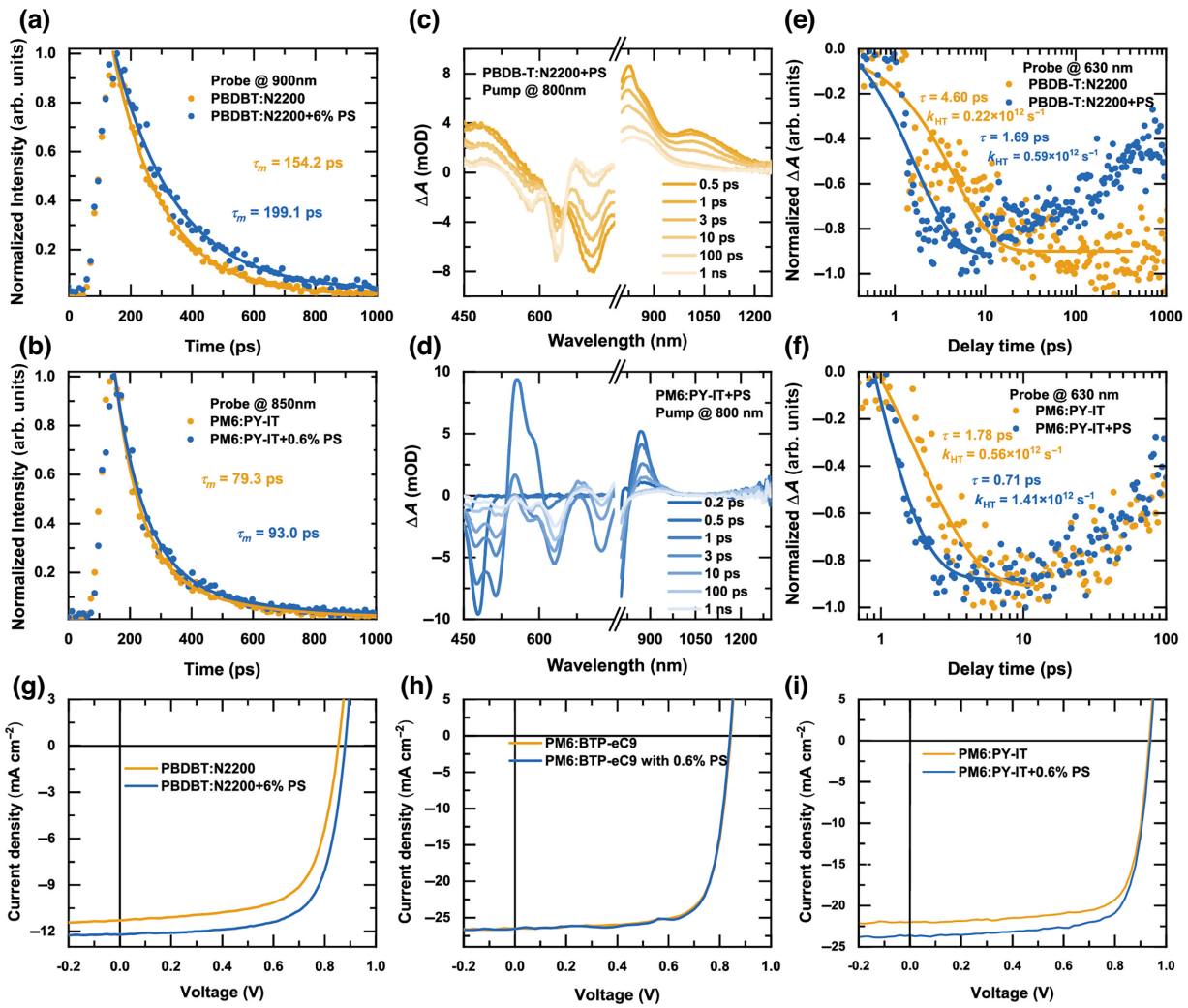


FIG. 6. (a),(b) Normalized time-resolved photoluminescence (TRPL) spectra of (a) PBDB-T:N2200 with different PS ratios and (b) PM6:PY-IT with different PS ratios. (c),(d) TA spectra at different probe delay times for (c) PBDB-T:N2200+PS and (d) PM6:PY-IT+PS. (e),(f) The dynamics of the rising signal of donor GSB in (e) the PM6:PY-IT system and (f) the PBDB-T:N2200 system. The solid curves are single-exponential fitting results. (g)–(i) Current density versus bias voltage (J - V) curves of the OSCs of (g) PBDB-T:N2200 with PS, (h) PM6:PY-IT with PS, and (i) PM6:BTP-eC9 with PS.

the donor and the acceptor in all-polymer systems. Meanwhile, the suppression of structural defects leads to a reduction in the density of the trap states. However, PS interacts with the donor in PM6:BTP-eC9 blends and disrupts the crystallinity and molecular stacking of the system.

IV. HOLE TRANSFER PROCESS AND DEVICE PERFORMANCES

The reduction of structural defects can influence the exciton dynamics. Time-resolved fluorescence lifetime imaging microscopy (FLIM) can be adopted to visualize the detailed dynamics of the exciton in BHJ films.

Figures 6(a) and 6(b) and Fig. S10 of the Supplemental Material [36] show the fluorescence-decay dynamics of each film. The decay profiles are fitted with a single-exponential decay function $I(t) = Ae^{-t/\tau}$. The detailed parameters are summarized in Table S6 of the Supplemental Material [36]. The fitted result is 79.3 ps for pristine PM6:PY-IT film, while a longer lifetime of 93 ps is observed in film blended with 0.6% PS. However, the fluorescence lifetimes decrease to 81.2 ps as the blending ratio increases to 1.0%. Similar phenomena can be observed in PBDB-T:N2200 blended with PS. The increased fluorescence lifetime indicates extension of the singlet exciton lifetime, which can be ascribed to the decreased trap-state density and more excitons being able to diffuse to the donor-acceptor interface [35]. The hole is a type of fermion

and it follows the Fermi-Dirac distribution. The average number of particles in a quantum state with energy ε at temperature T can be expressed as

$$f(\varepsilon) = \frac{1}{\exp\left[\frac{\varepsilon - \varepsilon_f}{kT}\right] + 1}, \quad (16)$$

where ε_f is the chemical potential and k is Boltzmann's constant. The reduction of structural defects can affect the hole distribution. The TA spectra were measured to explore the ultrafast hole transfer process (see Figs. S11 and S12 of the Supplemental Material [36]). A wavelength of 800 nm is used to selectively excite N2200 and PY-IT, and TA spectra for PBDB-T:N2200 and PM6:PY-IT probed in the visible region are shown in Figs. 6(c)–6(f). A clear ground-state-bleaching (GSB) signal of the donor is centered at around 640 nm (see Fig. S13 of the Supplemental Material [36]). In a previous report, Xiao *et al.* have suggested that the hole transfer process is mainly governed by the photoexcited intramoiety polaron pairs (iPPs), with a slower recombination process in all-polymer system, which is consistent with the results observed in this work [49]. For PBDB-T:N2200, the GSB signal of the donor is gradually generated as the ESA signal decays at 500 nm and spans a larger time scale, up to nanoseconds. This corresponds to the hole transfer process from the acceptor N2200 to the donor PBDB-T and the ESA signal at 500 nm is attributed to the iPPs of N2200 [35]. However, the photoinduced-absorption (PIA) signal at around 1200 nm corresponds to the iPPs of PY-IT and originates from the intramoiety state of charge-neutral excitations with weak interaction between spatially separated electrons and holes [50]. As the iPP signal decays, the GSB signal at 630 nm of donor PM6 emerges, which relates to the hole transfer process from PY-IT to PM6. In this work, the hole transfer process can be described by the Marcus theory, with [51]

$$\Delta G^+ = \frac{\lambda}{4} \left(1 + \frac{\Delta G^0}{\lambda}\right)^2, \quad (17)$$

where λ refers to the total reorganization energy, ΔG^0 is the change in the Gibbs free energy, and ΔG^+ is the activation energy. To further explore the hole transfer rate (k), diabatic representation can be combined with this theory as follows:

$$\begin{aligned} H &= T + \begin{bmatrix} V_1 & \Delta \\ \Delta & V_2 \end{bmatrix} \\ &\equiv T + \frac{1}{2}(V_1 + V_2) \parallel + \frac{1}{2}(V_1 - V_2)\sigma_z + \Delta\sigma_x \end{aligned} \quad (18)$$

and the hole transfer rate (k) can be described by

$$k = \frac{2\pi}{\hbar\sqrt{4\pi\lambda k_B T}} V^2 \exp\left(-\frac{(\lambda + \Delta G)}{4\lambda k_B T}\right), \quad (19)$$

where V refers to the electronic coupling between the initial and final states, ΔG is the change in the Gibbs free energy ($-\Delta G$ is the driving force and is usually positive), k_B is the Boltzmann constant, and T is the temperature. Considering that the GSB signal of the donor around 630 nm is gradually generated as the iPPs diffuse and dissociate at the interface, we then performed kinetic fitting of the GSB signal at 620 nm for both binary and PS-blended systems. The interfacial hole transfer (HT) rates in the different systems can be calculated by

$$k_{\text{HT}} = k_r - k_0, \quad (20)$$

where $k_r = 1/\tau_r$ and $k_0 = 1/\tau_0$. The quantum efficiency (QE) of photoinduced HT (in competition with intrinsic relaxation) can be estimated by

$$\text{QE} = \frac{k_{\text{HT}}}{(k_{\text{HT}} + k_0)}. \quad (21)$$

The results are shown in Table II and in Fig. S14 of the Supplemental Material [36]. We found that the hole transfer rate and efficiency were significantly increased after blending with PS. The hole transfer rate of PBDB-T:N2200 increased from 0.22×10^{12} to $0.59 \times 10^{12} \text{ s}^{-1}$ and the corresponding transfer efficiency rose from 90.53% to 96.25%. The hole transfer rate of PM6:PY-IT also rose from 0.56×10^{12} to $1.41 \times 10^{12} \text{ s}^{-1}$ and the corresponding transfer efficiency increased from 72.73% to 87.64%. The increase in the hole transfer efficiency should be ascribed to the significant decrease in the trap density of states [50]. Therefore, more iPPs can effectively diffuse to the interface of the acceptor, due to less trap-assisted recombination, and undergo dissociation, generating more free charges, which ultimately leads to a significant increase in the photocurrent as well as the external quantum efficiency (EQE) in the range of 300–800 nm.

We fabricated the devices based on PBDB-T:N2200, PM6:PY-IT, and PM6:BTP-eC9 with and without blending PS. The current density versus bias voltage ($J-V$) curves of the OSCs with the conventional structure and the EQE are shown in Figs. 6(g)–6(i) and in Fig. S15 of the Supplemental Material [36]. Compared with the control devices, the PCEs of the OSCs with PBDB-T:N2200 and PM6:PY-IT are substantially improved with the addition of PS. The maximum PCE of PBDB-T:N2200 is 7.48% when the addition ratio is 6.0 wt%. The PCE of PM6:PY-IT also reaches 16.72% when the addition ratio is 0.6 wt%. However, further addition of PS beyond 6.0 wt% and 0.6 wt% inversely decreases the PCE values of the devices. The detailed photovoltaic parameters for different addition ratios are shown in Table S7 of the Supplemental Material [36]. The dissociation probability ($P(E, T)$) is studied through the relationship between the photocurrent density (J_{ph}) and the effective voltage (V_{eff}). The $P(E, T)$ of the

TABLE II. Fitting parameters for the pump-fluence-dependent TA decay curves and the quantum efficiency.

System	τ (ps)	k_{HT} ($\times 10^{11} \text{s}^{-1}$)	QE (%)
N2200		0.23	
PBDB-T:N2200	4.60	0.22	90.53
PBDB-T:N2200 with PS	1.69	0.59	96.25
PY-IT	4.70	0.21	
PM6:PY-IT	1.78	0.56	72.73
PM6:PY-IT with PS	0.71	1.41	87.64

device with PS (93.27%) is higher than that of the control device (91.14%). It can be concluded that more charge carriers are accumulated at the electrodes for the device due to the improved exciton diffusion and charge separation (see Fig. S16 of the Supplemental Material [36]). For PBDB-T:N2200 and PM6:PY-IT, PS mainly acts between the donor and the acceptor and suppresses structural defects at the interface, which leads to an increase in FF and J_{SC} . In the case of PM6:BTP-eC9, the PS blending destroys the crystallinity of the system, so that the parameters are not significantly improved. This is consistent with our previous discussion of the variation in crystallinity and the trap-state density.

V. CONCLUSIONS

In this study, we have investigated the impact of blending PS with the photoactive layer in order to regulate the structural-evolution process and suppress structural defects in OSCs. Our results demonstrate that the blending of PS leads to a longer solidification process and a significant decrease in the density of the trap states in the all-polymer systems PBDB-T:N2200 and PM6:PY-IT. However, the energy levels occupied by the trap states do not change significantly. Interestingly, in the case of the OSCs based on the nonfullerene small-molecule acceptor BTP-eC9, blending with the insulating polymer does not significantly reduce the trap states. By reducing the density of the trap states, we have observed improvements in the exciton lifetime, hole transfer rate, and overall efficiency, leading to lower photocurrent loss and higher performance in the OSCs. Our findings provide a fundamental understanding of the effect of insulating polymers on the density of the trap states in the active layer and offer a new perspective on suppressing trap-assisted recombination in all-polymer OSCs.

ACKNOWLEDGMENTS

This work was supported by the National Natural Science Foundation of China (Grant No. 52073162) and the Major Program of the Natural Science Foundation of Shandong Province (Grant No. ZR2019ZD43). X.T.H. also

acknowledges support from the ARC Centre of Excellence in Exciton Science (CE170100026). We would like to thank the Analytical Center for Structural Constituent and Physical Property of the Core Facilities Sharing Platform, Shandong University, for the femtosecond transient-absorption-spectroscopy (TAS) system.

- [1] Y. Li, G. Xu, C. Cui, and Y. Li, Flexible and semitransparent organic solar cells, *Adv. Energy Mater.* **8**, 1701791 (2018).
- [2] J. Wang, C. Han, J. Han, F. Bi, X. Sun, S. Wen, C. Yang, C. Yang, X. Bao, and J. Chu, Synergetic strategy for highly efficient and super flexible thick-film organic solar cells, *Adv. Energy Mater.* **12**, 1701791 (2022).
- [3] X. Duan, W. Song, J. Qiao, X. Li, Y. Cai, H. Wu, J. Zhang, X. Hao, Z. Tang, Z. Ge, F. Huang, and Y. Sun, Ternary strategy enabling high-efficiency rigid and flexible organic solar cells with reduced non-radiative voltage loss, *Energy Environ. Sci.* **15**, 1563 (2022).
- [4] Y. Cui, H. Yao, J. Zhang, K. Xian, T. Zhang, L. Hong, Y. Wang, Y. Xu, K. Ma, C. An, C. He, Z. Wei, F. Gao, and J. Hou, Single-junction organic photovoltaic cells with approaching 18% efficiency, *Adv. Mater.* **32**, 1908205 (2020).
- [5] P. Bi, S. Zhang, J. Ren, Z. Chen, Z. Zheng, Y. Cui, J. Wang, S. Wang, T. Zhang, J. Li, Y. Xu, J. Qin, C. An, W. Ma, X. Hao, and J. Hou, A high-performance nonfused wide-bandgap acceptor for versatile photovoltaic applications, *Adv. Mater.* **34**, 2108090 (2022).
- [6] J. Wang, M. Zhang, J. Lin, Z. Zheng, L. Zhu, P. Bi, H. Liang, X. Guo, J. Wu, Y. Wang, L. Yu, J. Li, J. Lv, X. Liu, F. Liu, J. Hou, and Y. Li, An asymmetric wide-bandgap acceptor simultaneously enabling highly efficient single-junction and tandem organic solar cells, *Energy Environ. Sci.* **15**, 1585 (2022).
- [7] W. Gao, F. Qi, Z. Peng, F. R. Lin, K. Jiang, C. Zhong, W. Kaminsky, Z. Guan, C. S. Lee, T. J. Marks, H. Ade, and A. K. Jen, Achieving 19% power conversion efficiency in planar-mixed heterojunction organic solar cells using a pseudosymmetric electron acceptor, *Adv. Mater.* **34**, 2202089 (2022).
- [8] C. He, Y. Pan, Y. Ouyang, Q. Shen, Y. Gao, K. Yan, J. Fang, Y. Chen, C.-Q. Ma, J. Min, C. Zhang, L. Zuo, and H. Chen, Manipulating the D:A interfacial energetics and intermolecular packing for 19.2% efficiency organic photovoltaics, *Energy Environ. Sci.* **15**, 2537 (2022).
- [9] Y. Su, L. Zhang, Z. Ding, Y. Zhang, Y. Wu, Y. Duan, Q. Zhang, J. Zhang, Y. Han, Z. Xu, R. Zhang, K. Zhao, and S. Liu, Carrier generation engineering toward 18% efficiency organic solar cells by controlling film microstructure, *Adv. Energy Mater.* **12**, 2103940 (2022).
- [10] R. Sun, Y. Wu, X. Yang, Y. Gao, Z. Chen, K. Li, J. Qiao, T. Wang, J. Guo, C. Liu, X. Hao, H. Zhu, and J. Min, Single-junction organic solar cells with 19.17% efficiency enabled by introducing one asymmetric guest acceptor, *Adv. Mater.* **34**, 2110147 (2022).
- [11] Y. Wei, Z. Chen, G. Lu, N. Yu, C. Li, J. Gao, X. Gu, X. Hao, G. Lu, Z. Tang, J. Zhang, Z. Wei, X. Zhang, and H.

- Huang, Binary organic solar cells breaking 19% via manipulating the vertical component distribution, *Adv. Mater.* **34**, 2204718 (2022).
- [12] L. Zhu, M. Zhang, J. Xu, C. Li, J. Yan, G. Zhou, W. Zhong, T. Hao, J. Song, X. Xue, Z. Zhou, R. Zeng, H. Zhu, C. C. Chen, R. C. I. MacKenzie, Y. Zou, J. Nelson, Y. Zhang, Y. Sun, and F. Liu, Single-junction organic solar cells with over 19% efficiency enabled by a refined double-fibril network morphology, *Nat. Mater.* **21**, 656 (2022).
- [13] Y. Cheng, B. Huang, X. Huang, L. Zhang, S. Kim, Q. Xie, C. Liu, T. Heumuller, Z. Liu, Y. Zhang, F. Wu, C. Yang, C. J. Brabec, Y. Chen, and L. Chen, Oligomer-assisted photoactive layers enable > 18% efficiency of organic solar cells, *Angew. Chem., Int. Ed. Engl.* **134**, 202200329 (2022).
- [14] K. N. Zhang, X. Y. Du, Z. H. Chen, T. Wang, Z. Q. Yang, H. Yin, Y. Yang, W. Qin, and X. T. Hao, Reducing limitations of aggregation-induced photocarrier trapping for photovoltaic stability via tailoring intermolecular electron-phonon coupling in highly efficient quaternary polymer solar cells, *Adv. Energy Mater.* **12**, 2103371 (2021).
- [15] K. Chong, X. Xu, H. Meng, J. Xue, L. Yu, W. Ma, and Q. Peng, Realizing 19.05% efficiency polymer solar cells by progressively improving charge extraction and suppressing charge recombination, *Adv. Mater.* **34**, 2109516 (2022).
- [16] Y. Wu, Q. Fan, B. Fan, F. Qi, Z. Wu, F. R. Lin, Y. Li, C.-S. Lee, H. Y. Woo, H.-L. Yip, and A. K. Y. Jen, Non-fullerene acceptor doped block copolymer for efficient and stable organic solar cells, *ACS Energy Lett.* **7**, 2196 (2022).
- [17] S. Li, Y. Ding, L. Xu, W. Zhao, J. Zhang, J. Qin, Y. Zhang, J. Zhao, C. He, Q. Peng, and J. Hou, The key role of subtle substitution for a high-performance ester-modified oligothiophene-based polymer used in photovoltaic cells, *Chin. J. Chem.* **40**, 2867 (2022).
- [18] J. Yang, B. Liu, J. W. Lee, Y. Wang, H. Sun, Z. Chen, Q. Bai, B. J. Kim, Y. Jiang, L. Niu, and X. Guo, Revisiting the bithiophene imide-based polymer donors: Molecular aggregation and orientation control enabling new polymer donors for high-performance all-polymer solar cells, *Chin. J. Chem.* **40**, 2900 (2022).
- [19] H. F. Haneef, A. M. Zeidell, and O. D. Jurchescu, Charge carrier traps in organic semiconductors: A review on the underlying physics and impact on electronic devices, *J. Mater. Chem. C* **8**, 759 (2020).
- [20] M. Azzouzi, J. Yan, T. Kirchartz, K. Liu, J. Wang, H. Wu, and J. Nelson, Nonradiative energy losses in bulk-heterojunction organic photovoltaics, *Phys. Rev. X* **8**, 031055 (2018).
- [21] S. Wheeler, F. Deledalle, N. Tokmoldin, T. Kirchartz, J. Nelson, and J. R. Durrant, Influence of surface recombination on charge-carrier kinetics in organic bulk heterojunction solar cells with nickel oxide interlayers, *Phys. Rev. Appl.* **4**, 024020 (2015).
- [22] H. Yan, J. G. Manion, M. Yuan, F. P. Garcia de Arquer, G. R. McKeown, S. Beaupre, M. Leclerc, E. H. Sargent, and D. S. Seferos, Increasing polymer solar cell fill factor by trap-filling with F4-TCNQ at parts per thousand concentration, *Adv. Mater.* **28**, 6491 (2016).
- [23] C. R. McNeill and N. C. Greenham, Charge transport dynamics of polymer solar cells under operating conditions: Influence of trap filling, *Appl. Phys. Lett.* **93**, 425 (2008).
- [24] P. Mondelli, F. Silvestri, L. Ciammaruchi, E. Solano, E. Beltrán-Gracia, E. Barrena, M. Riede, and G. Morse, A liquid-crystalline non-fullerene acceptor enabling high-performance organic solar cells, *J. Mater. Chem. A* **9**, 26917 (2021).
- [25] F. Deledalle, T. Kirchartz, M. S. Vezie, M. Campoy-Quiles, P. Shakya Tuladhar, J. Nelson, and J. R. Durrant, Understanding the effect of unintentional doping on transport optimization and analysis in efficient organic bulk-heterojunction solar cells, *Phys. Rev. X* **5**, 011032 (2015).
- [26] Z. Peng, Y. Zhang, X. Sun, W. Zhao, F. Bian, Y. Geng, L. Ye, and C. Yang, Real-time probing and unraveling the morphology formation of blade-coated ternary nonfullerene organic photovoltaics with *in situ* x-ray scattering, *Adv. Funct. Mater.* **33**, 2213248 (2023).
- [27] H. Zhao, J. Xue, H. Wu, B. Lin, Y. Cai, K. Zhou, D. Yun, Z. Tang, and W. Ma, High-performance green thick-film ternary organic solar cells enabled by crystallinity regulation, *Adv. Funct. Mater.* **33**, 2210534 (2022).
- [28] J. Xue, H. Zhao, B. Lin, Y. Wang, Q. Zhu, G. Lu, B. Wu, Z. Bi, X. Zhou, C. Zhao, G. Lu, K. Zhou, and W. Ma, Nonhalogenated dual-slot-die processing enables high-efficiency organic solar cells, *Adv. Mater.* **34**, 2202659 (2022).
- [29] L. Chen, J. Yi, R. Ma, L. Ding, T. A. Dela Pena, H. Liu, J. Chen, C. Zhang, C. Zhao, W. Lu, Q. Wei, B. Zhao, H. Hu, J. Wu, Z. Ma, X. Lu, M. Li, G. Zhang, G. Li, and H. Yan, An isomeric solid additive enables high-efficiency polymer solar cells developed using a benzo-difuran-based donor polymer, *Adv. Mater.* **35**, 2301231 (2023).
- [30] D. Abbaszadeh, A. Kunz, G. A. Wetzelraer, J. J. Michels, N. I. Craciun, K. Koynov, I. Lieberwirth, and P. W. Blom, Elimination of charge carrier trapping in diluted semiconductors, *Nat. Mater.* **15**, 628 (2016).
- [31] M. Wang, S. Liu, P. You, N. Wang, G. Tang, Q. Miao, and F. Yan, Insulating polymers for enhancing the efficiency of nonfullerene organic solar cells, *Solar RRL* **4**, 2000013 (2020).
- [32] T. Wang, J.-Q. Liu, and X.-T. Hao, Recent progress of organic solar cells with insulating polymers, *Solar RRL* **4**, 2000539 (2020).
- [33] A. D. Scaccabarozzi and N. Stingelin, Semiconducting:insulating polymer blends for optoelectronic applications—a review of recent advances, *J. Mater. Chem. A* **2**, 10818 (2014).
- [34] T. Wang, M. S. Niu, Z. C. Wen, Z. N. Jiang, C. C. Qin, X. Y. Wang, H. Y. Liu, X. Y. Li, H. Yin, J. Q. Liu, and X. T. Hao, High-efficiency thickness-insensitive organic solar cells with an insulating polymer, *ACS Appl. Mater. Interfaces* **13**, 11134 (2021).
- [35] T. Wang, Z.-C. Wen, L.-H. Xu, C.-C. Qin, H. Yin, J.-Q. Liu, and X.-T. Hao, One-micron-thick organic indoor light harvesters with low photocurrent loss and fill factors over 67%, *J. Mater. Chem. A* **9**, 13515 (2021).
- [36] See the Supplemental Material at <http://link.aps.org/supplemental/10.1103/PRXEnergy.2.043012> for the materials; fabrication methods of OPV cells; photoluminescence and

- time-resolved photoluminescence spectra; transient absorption spectra; the hole transfer rate and efficiency; 2D GIWAXS patterns and corresponding 1D profiles from GIWAXS patterns; 2D GISAXS patterns and corresponding 1D profiles from GISAXS patterns; time-dependent contour maps of UV-vis absorption spectra; glycerin and water contact angles of different materials; bias-dependent capacitance-frequency spectra; the trap-state density; transient photocurrents at different temperatures; and device parameters with different systems.
- [37] Q. Zhang, H. Zhang, Z. Wu, C. Wang, R. Zhang, C. Yang, F. Gao, S. Fabiano, H. Y. Woo, M. Ek, X. Liu, and M. Fahlman, Natural product betulin-based insulating polymer filler in organic solar cells, *Solar RRL* **6**, 2200381 (2022).
- [38] Y. Xiao and X. Lu, Morphology of organic photovoltaic non-fullerene acceptors investigated by grazing incidence x-ray scattering techniques, *Materials Today Nano* **5**, 100030 (2019).
- [39] J. Wang, X. Ma, J. Wang, R. Ming, Q. An, J. Zhang, C. Yang, and F. Zhang, Two well-compatible acceptors with efficient energy transfer enable ternary organic photovoltaics exhibiting a 13.36% efficiency, *Small* **15**, 1902602 (2019).
- [40] W. Li, M. Chen, J. Cai, E. L. K. Spooner, H. Zhang, R. S. Gurney, D. Liu, Z. Xiao, D. G. Lidzey, L. Ding, and T. Wang, Molecular order control of non-fullerene acceptors for high-efficiency polymer solar cells, *Joule* **3**, 819 (2019).
- [41] Z. Liang, J. Tong, H. Li, Y. Wang, N. Wang, J. Li, C. Yang, and Y. Xia, The comprehensive utilization of the synergistic effect of fullerene and non-fullerene acceptors to achieve highly efficient polymer solar cells, *J. Mater. Chem. A* **7**, 15841 (2019).
- [42] T. Wang, M.-S. Niu, J.-J. Guo, K.-N. Zhang, Z.-C. Wen, J.-Q. Liu, C.-C. Qin, and X.-T. Hao, 3D charge transport pathway in organic solar cells via incorporation of discotic liquid crystal columns, *Solar RRL* **4**, 000047 (2020).
- [43] S. Dong, T. Jia, K. Zhang, J. Jing, and F. Huang, Single-component non-halogen solvent-processed high-performance organic solar cell module with efficiency over 14%, *Joule* **4**, 2004 (2020).
- [44] C. D. Christ, A. E. Mark, and W. F. van Gunsteren, Basic ingredients of free energy calculations: A review, *J. Comput. Chem.* **31**, 1569 (2010).
- [45] A. Villa and A. E. Mark, Calculation of the free energy of solvation for neutral analogs of amino acid side chains, *J. Comput. Chem.* **23**, 548 (2002).
- [46] S. Khelifi, K. Decock, J. Lauwaert, H. Vrielinck, D. Spoltore, F. Piersimoni, J. Manca, A. Belghachi, and M. Burgelman, Investigation of defects by admittance spectroscopy measurements in poly (3-hexylthiophene):(6,6)-phenyl C₆₁-butyric acid methyl ester organic solar cells degraded under air exposure, *J. Appl. Phys.* **110**, 094509 (2011).
- [47] M. Zhang, L. Zhu, T. Hao, G. Zhou, C. Qiu, Z. Zhao, N. Hartmann, B. Xiao, Y. Zou, W. Feng, H. Zhu, M. Zhang, Y. Zhang, Y. Li, T. P. Russell, and F. Liu, High-efficiency organic photovoltaics using eutectic acceptor fibrils to achieve current amplification, *Adv. Mater.* **33**, 2007177 (2021).
- [48] T. Walter, R. Herberholz, C. Müller, and H. W. Schock, Determination of defect distributions from admittance measurements and application to Cu(In,Ga)Se₂ based heterojunctions, *J. Appl. Phys.* **80**, 4411 (1996).
- [49] R. Wang, Y. Yao, C. Zhang, Y. Zhang, H. Bin, L. Xue, Z. G. Zhang, X. Xie, H. Ma, X. Wang, Y. Li, and M. Xiao, Ultrafast hole transfer mediated by polaron pairs in all-polymer photovoltaic blends, *Nat. Commun.* **10**, 398 (2019).
- [50] F. Z. Cui, Z. H. Chen, J. W. Qiao, T. Wang, G. H. Lu, H. Yin, and X. T. Hao, Ternary-assisted sequential solution deposition enables efficient all-polymer solar cells with tailored vertical-phase distribution, *Adv. Funct. Mater.* **32**, 2200478 (2022).
- [51] G. Zhou, M. Zhang, Z. Chen, J. Zhang, L. Zhan, S. Li, L. Zhu, Z. Wang, X. Zhu, H. Chen, L. Wang, F. Liu, and H. Zhu, Marcus hole transfer governs charge generation and device operation in nonfullerene organic solar cells, *ACS Energy Lett.* **6**, 2971 (2021).